Journal of Alloys and Compounds 1041 (2025) 183862

Contents lists available at ScienceDirect

Journal of Alloys and Compounds

journal homepage: www.elsevier.com/locate/jalcom

Synergistic enhancement of corrosion resistance and mechanical properties of extruded Mg-Y-Al alloys by regulating the LPSO phase

Yiwen Chen [a,b], Yuyang Chen [b,*], Chao Wu [c], Jie Wang [b], Chao Yang [b,*], Paul K. Chu [d], Xiaoqin Zeng [b]

[a] School of Intelligent Manufacturing, Jiangsu Key Laboratory of Advanced Food Manufacturing Equipment and Technology, Jiangnan University, Wuxi, China
[b] National Engineering Research Center of Light Alloy Net Forming and State Key Laboratory of Metal Matrix Composite, Shanghai Jiao Tong University, Shanghai, China
[c] Jiangsu Key Laboratory of Advanced Structural Materials and Application Technology, Nanjing Institute of Technology, Nanjing, China
[d] Department of Physics, Department of Materials Science & Engineering, and Department of Biomedical Engineering, City University of Hong Kong, Tat Chee Avenue, Kowloon, Hong Kong, China

ARTICLE INFO

Keywords:
Mg alloys
LPSO phase
Corrosion resistance
Mechanical properties
Quasi-passivating corrosion film
Electrochemical analysis

ABSTRACT

The persistent tradeoff between strength and corrosion resistance has limited the widespread commercial application of Mg alloys. In this study, an extruded Mg-5.5Y-0.9Al (wt%, WA61) alloy is fabricated by tailoring the formation of the long-period stacking ordered (LPSO) phase by pre-extrusion heat treatment. The LPSO phase enhances both the mechanical strength and corrosion resistance. The WA61–400-E alloy, featuring a refined grain size of 6.74 μm and 7 % volume fraction of the LPSO phase, exhibits a yield stress (YS) of 225 ± 8 MPa and corrosion rate of 0.10 mm·y^{-1} in the 3.5 wt% NaCl solution. In contrast, the WA61–500-E alloy without LPSO and a coarser grain size (16.93 μm) displays a smaller YS (133 ± 6 MPa) and larger corrosion rate (0.36 mm·y^{-1}). The improved corrosion resistance of WA61–400-E is attributed to the rapid formation of a compact, quasi-passivating corrosion film due to grain refinement and suppression of the formation of the Al_2Y phase. The results underscore the effectiveness of LPSO phase engineering as a viable strategy to achieve simultaneous improvement of strength and corrosion resistance for Mg-Y-Al alloys.

1. Introduction

Mg alloys have attracted increasing attention as lightweight structural components in automotive and aerospace industries due to their low density and superior damping capacity [1]. However, widespread applications remain constrained by the poor corrosion resistance and suboptimal mechanical properties [1–5]. Grain refinement can improve strength through the Hall-Petch effect and also ductility by accommodating multiple grains [6,7]. The grain size influences the corrosion properties of Mg alloys, as grain boundaries serve as physical barriers impeding corrosion propagation [8,9]. Therefore, grain refinement can potentially improve both the corrosion resistance and mechanical properties of Mg alloys.

Thermo-mechanical processing such as the hot extrusion is a common method to refine the grain size in Mg alloys, such as the hot-extrusion process [10]. The coarse grains in cast Mg alloys can be refined to 2–30 μm by dynamic recrystallization (DRX) during hot extrusion. In this case, the second phase, especially the lamellar precipitate, can decrease the DRX grain size by particle stimulated nucleation (PSN) and hinder grain boundary migration [11–13]. The long-period stacking ordered (LPSO) phase is a typical lamellar precipitate phase in Mg-X^l-X^s alloys (X^l = Y, Gd, Er, etc.; X^L = Zn, Cu, Al, etc.) [14]. The LPSO phase can suppress DRX of the α-Mg phase during hot extrusion from two aspects: (i) The partial LPSO phase can break into small particles during extrusion [15]. The (0002) plane of the LPSO and α-Mg phase is completely coherent, and therefore, the broken phase can act as nucleation particles based on the edge-edge matching (E2EM) model [16]. This provides a way for the nucleation of DRX α-Mg grains. (ii) Some LPSO phases with nano-scale widths can serve as pinning sites to restrict the growth of DRX grains [15]. Li et al. [17] have proposed a modified Zener model to evaluate the pinning effect of the LPSO phases on the GB movement in the α-Mg phase. In the model, the N-LPSO phase displays significant pinning effects on the GB movement of the DRXed grains rather than other GB pinning phases with micrometer-scale and near-spherical shape, such as the Al_2Ca [18] or Al_2Y [19] (radius of 5–10 μm). Hence, the LPSO phase can be introduced to Mg alloys to

* Corresponding authors.
E-mail addresses: yuyangchen0@sjtu.edu.cn (Y. Chen), chaoyang0315@163.com (C. Yang).

https://doi.org/10.1016/j.jallcom.2025.183862
Received 2 August 2025; Received in revised form 16 September 2025; Accepted 17 September 2025
Available online 18 September 2025

refine the grain size during hot extrusion.

In addition to refining the DRX grain size, the LPSO phase strengthens Mg alloys by mechanisms such as short-fiber reinforcement strengthening [20–22] and precipitate strengthening [15,23,24]. However, introducing the LPSO phase inherently exacerbates galvanic corrosion [25,26]. For instance, the corrosion rate of the Mg-Y-Zn alloy with a 3.6 % volume fraction of LPSO (V_f(LPSO)) increases from 0.51 mg/cm^2/day to 4.5 mg/cm^2/day when V_f(LPSO) goes up to 20.3 % [27]. Zhou et al. [28] have demonstrated that the LPSO phase exhibits a substantial potential difference (PD) of ~ 250 mV relative to the α-Mg matrix. Zhang et al. [26] have also reported that corrosion pits are frequently initiated at the LPSO/α-Mg interfaces, subsequently developing into prominent localized etched holes and undermining the corrosion resistance of Mg alloys. Therefore, despite the benefits offered by grain refinement, the introduction of the LPSO phase intensifies galvanic corrosion, indicating that enhancing corrosion resistance by merely incorporating the LPSO phase can be misleading.

The objective of this study is to clarify how the LPSO phase affects corrosion and to achieve simultaneous improvements in corrosion resistance and mechanical properties of extruded Mg alloys. We focus on Mg–Y–Al alloys because the LPSO fraction and morphology can be precisely tuned by annealing [14], and this system can form quasi-passivating films that mitigate micro-galvanic attack [29,30]. Building on our previous CALPHAD-guided design of high strength–ductility Mg–Y–Al alloys [15], the present work targets high strength with enhanced corrosion resistance via microstructure control and elucidates the underlying mechanism. Comprehensive microstructural, mechanical, and electrochemical analyses establish a viable route to overcome the conventional strength–corrosion trade-off in Mg alloys.

2. Experimental procedures

The ingots of the nominal composition of Mg-5.5Y-0.9Al (wt%, WA61) alloy were melted in a resistance furnace under flowing CO_2/SF_6. The raw materials are high-purity Mg (> 99.9 wt%), Al (> 99.999 wt%), and Mg-30Y (wt%) master alloys. The chemical composition of the as-cast WA61 ingot was determined by inductively coupled plasma emission spectrometry (ICP-AES, Thermo Fisher Scientific), and the results are listed in Table 1. Prior to extrusion, the WA61 ingots were homogenized at 400 ℃ (WA61–400) and 500 ℃ (WA61–500) for 24 h. Hot extrusion was then carried out at 350 ℃ using an extrusion ratio of 18:1 to produce the WA61–400-E and WA61–500-E alloys, respectively.

The phases of WA61–400-E and WA61–500-E were determined by X-ray diffraction (XRD, MAXima_X-7000) with Cu K_α radiation in the 2θ range between 10° and 80° at a rate of 3°/min. A scanning electron microscope (SEM, HITACHI SU8600), equipped with backscattered electron (BSE), energy-dispersive X-ray spectroscopy (EDS), and electron backscatter diffraction (EBSD) was used. The samples for BSE and EBSD were polished progressively with abrasive papers of 320, 1200, 3000, and 7000 grit and polished electrochemically in a solution comprising 10 vol% perchloric acid and alcohol (voltage: 30 V, current: 0.2–0.4 mA, temperature: −30 ℃ and time: 100–150 s). The pole figure (PF), inverse PF (IPF) maps, and statistical analyses of the DRX grain size were conducted using the Aztec Crystal software. The Talos F200X transmission electron microscope (TEM) was used to obtain high-resolution images at 200 kV. The TEM specimens were thinned to 60–70 μm, twin-jet electropolished with a 4 wt% perchloric acid in ethanol, and ion milled (PIPs 695). The surface morphology of the samples with and without corrosion products was examined by confocal laser scanning microscopy (CLSM, Olympus Lext OLS5100) and SEM (both plain and cross-sectional views). The composition of the corrosion products was analyzed by X-ray photoelectron spectroscopy (XPS) on the Thermo Fisher Scientific Nexsa using monochromatic Al-K_α radiation. Volta potential fluctuations in the studied Mg-Y-Al alloys with LPSO phases were assessed using scanning Kelvin probe force microscopy (SKPFM, Dimension Icon, Bruker), revealing trends in surface morphology and potential differences.

Table 1
Chemical composition of the WA61 alloy determined by ICP-AES.

Sample no.	Y	Al	Fe	Ni	Cu	Mg
WA61	5.74	0.872	0.016	< 0.0005	< 0.0005	bal.

The electrochemical tests were carried out on a Gamry electrochemical workstation with a conventional three-electrode cell configuration. The saturated calomel electrode (SCE) served as the reference electrode, a high-purity platinum sheet functioned as the counter electrode, and the specimen under investigation was the working electrode. The electrochemical measurements were conducted in a corrosion cell containing 200 mL of 3.5 wt% NaCl, and the electrode had a standard exposure area of 1 cm^2. Prior to electrochemical tests, the specimens were mechanically ground with abrasive papers up to 7000 grits. Potentiodynamic polarization was conducted from −5 mV relative to the open-circuit potential (OCP) up to 1.6 V vs. SCE. Electrochemical impedance spectroscopy (EIS) was performed in the frequency range between 10^5 Hz and 10^{-2} Hz with an excitation amplitude of ±10 mV. The electrochemical data were analyzed by the ZView software.

The long-term corrosion properties were determined by immersion tests and electrochemical methods. The immersion tests were conducted at 25 ℃ in a neutral 3.5 wt% NaCl solution for 14 days. The cuboid specimens measuring 12 mm × 8 mm × 4 mm were polished with up to 7000-grit abrasive papers before the test. The samples were then suspended with nylon strings in 800 mL of 3.5 wt% NaCl beneath inverted glass funnels. The hydrogen gas (H_2) evolved during corrosion was collected with burettes. Each measurement was performed in triplicate to ensure data reliability. After immersion, the corrosion products were removed using a solution consisting of 200 g/L chromic acid, 10 g/L silver nitrate, and 20 g/L barium nitrate, in accordance with the ASTM G1–03 standard. After drying, the samples were reweighed. The average corrosion rate (CR) in mm y^{-1} was calculated by the following formula:

$$CR = \frac{8.76 \times 10^4 \times \Delta m}{\rho \times A \times t}$$

where Δm is the mass loss (g), is the density of the alloy (g/cm^3), A is the surface area (cm^2), and t is the immersion time (h).

The tensile tests were performed on a universal testing machine (MTS, model C44.304) using a constant displacement rate of 0.5 mm/min. The dog-bone-shaped tensile specimens with dimensions of 12 mm × 3 mm × 1.4 mm were prepared. To obtain better statistics, each tensile specimen was tested three times.

3. Results

3.1. Phase composition and microstructure

The phase and microstructure of WA61–400-E and WA61–500-E alloys are presented in Fig. 1. The XRD patterns (Fig. 1a) exhibit common diffraction peaks corresponding to the α-Mg and Al_2Y phases in both alloys. The diffraction peaks at 2θ of 30° ~ 40° from the WA61–400-E alloy correspond to the 18R-type LPSO phase [31]. The microstructure of WA61–400-E alloy is depicted in Fig. 1b-e. The extrusion direction (ED) is parallel to the horizontal direction. Three distinctive morphological features are observed based on contrast variations: (i) dark regions corresponding to the α-Mg matrix; (ii) bright regions composed of fine, particle-like Al_2Y phases aligned with the ED; and (iii) grey regions showing irregular and lamellar structures identified as block LPSO (B-LPSO, microscale width) and a nano-scale width LPSO (N-LPSO). Both the B-LPSO and N-LPSO phases exhibit alignment parallel to the ED (Fig. 1b and c), which is estimated to be ~7 % in WA61–400-E. Some N-LPSO phases are kinked during extrusion deformation, as indicated by the dashed box in Fig. 1c. The dynamically

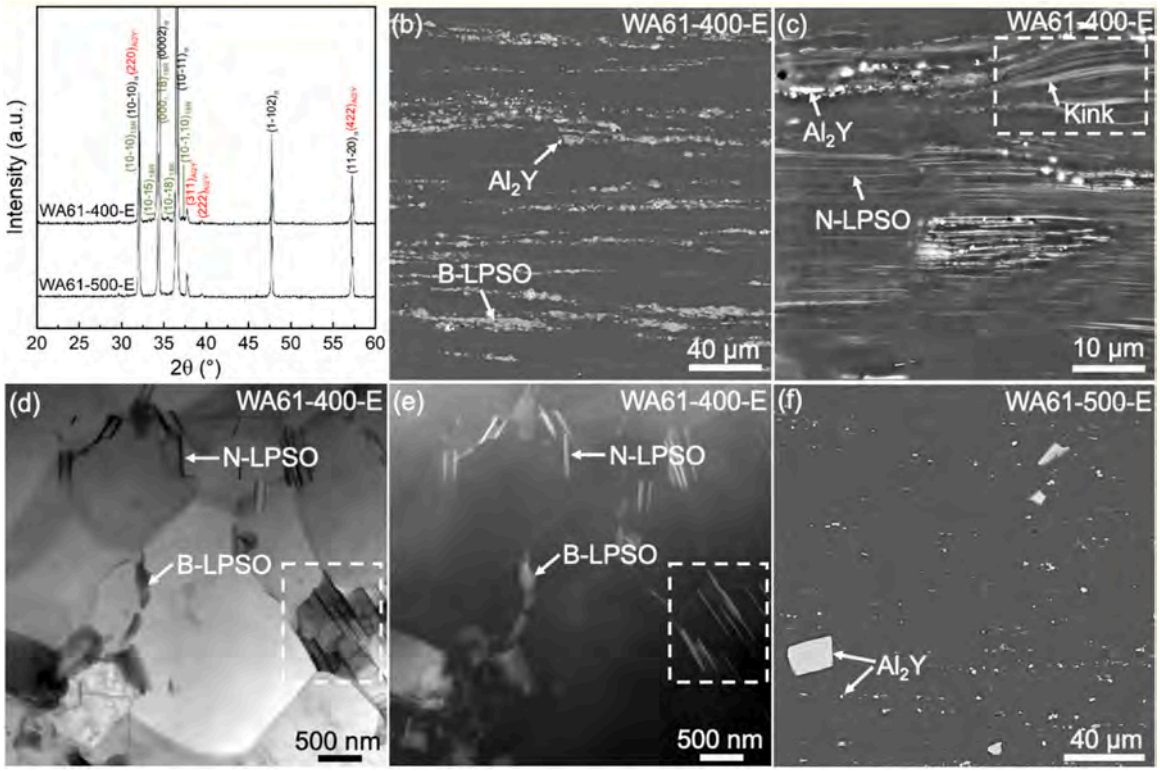

Fig. 1. (a) Phase and microstructure of WA61–400-E and WA61–500-E alloys: (a) XRD patterns; (b, c) BSE images of WA61–400-E showing that the extrusion direction (ED) is parallel to the horizontal direction; (d) Bright-field scanning TEM (BF-STEM) image of WA61–400-E; (e) Dark-field scanning TEM (DF-STEM) image of WA61–400-E; (f) BSE image of WA61–500-E showing that the ED direction is horizontal.

recrystallized (DRX) grains are analyzed by bright-field (BF-TEM) and dark-field (DF-TEM) imaging (Fig. 1d and e). The N-LPSO phases are pinned in the DRX grain boundaries (highlighted by the dashed box in Fig. 1d). In addition, the fragmented B-LPSO phases are dispersed within the grains, potentially acting as nucleation sites *via* particle-stimulated nucleation (PSN). Upon increasing the homogenization temperature to 500 °C before extrusion, WA61–500-E shows only the α-Mg and Al_2Y phases without B-LPSO and N-LPSO phases. In addition, the experimentally measured volume fraction of Al_2Y is 0.31 in WA61–400-E and 1.10 in WA61–500-E. The thermodynamic stability of the LPSO phase decreases with annealing temperature, in agreement with the CALPHAD-type calculations and consistent thermodynamic description of the Mg-Y-Al system (Fig. 2) [14].

The IPF maps illustrate that the WA61–400-E alloy with LPSO phases has a bimodal microstructure composed of equiaxed DRX grains and elongated non-DRX grains (Fig. 3a). In contrast, WA61–500-E has a fully equiaxed DRX grain structure (Fig. 3d). Fig. 3b and e show the DRX grain-size distributions of WA61–400-E and WA61–500-E, respectively. The average DRX grain sizes are 6.74 μm for WA61–400-E containing LPSO phases and 16.93 μm for WA61–500-E without LPSO phases.

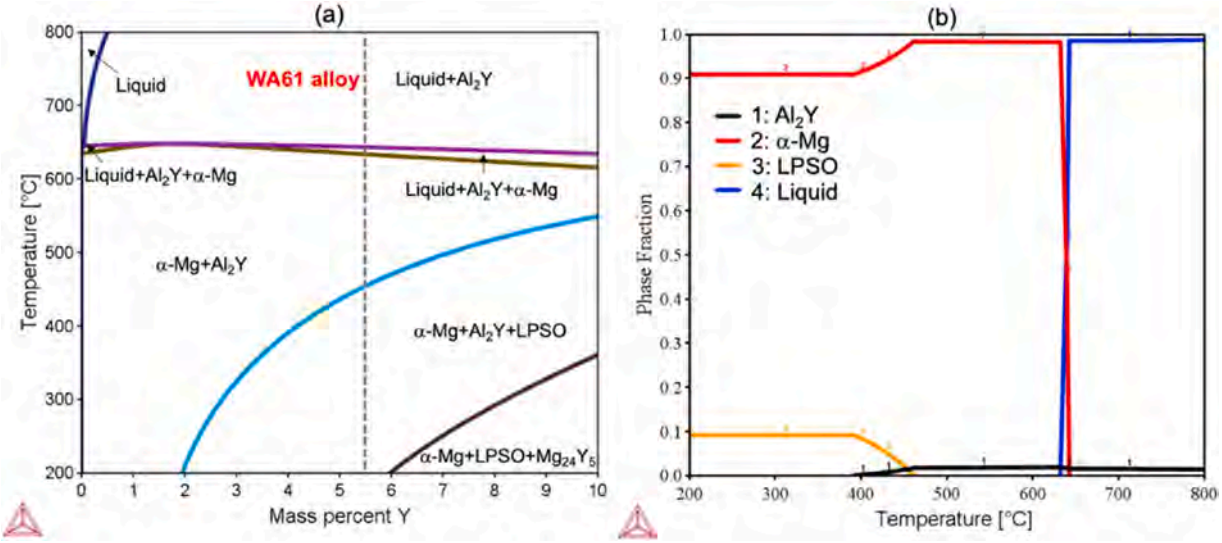

Fig. 2. Phase diagram derived by the CALPHAD method with the Mg-Y-Al description [14,15]: (a) Polythermal-section diagram of the Mg-xY-0.9Al system and (b) Phase-fraction diagram of the WA61 alloy.

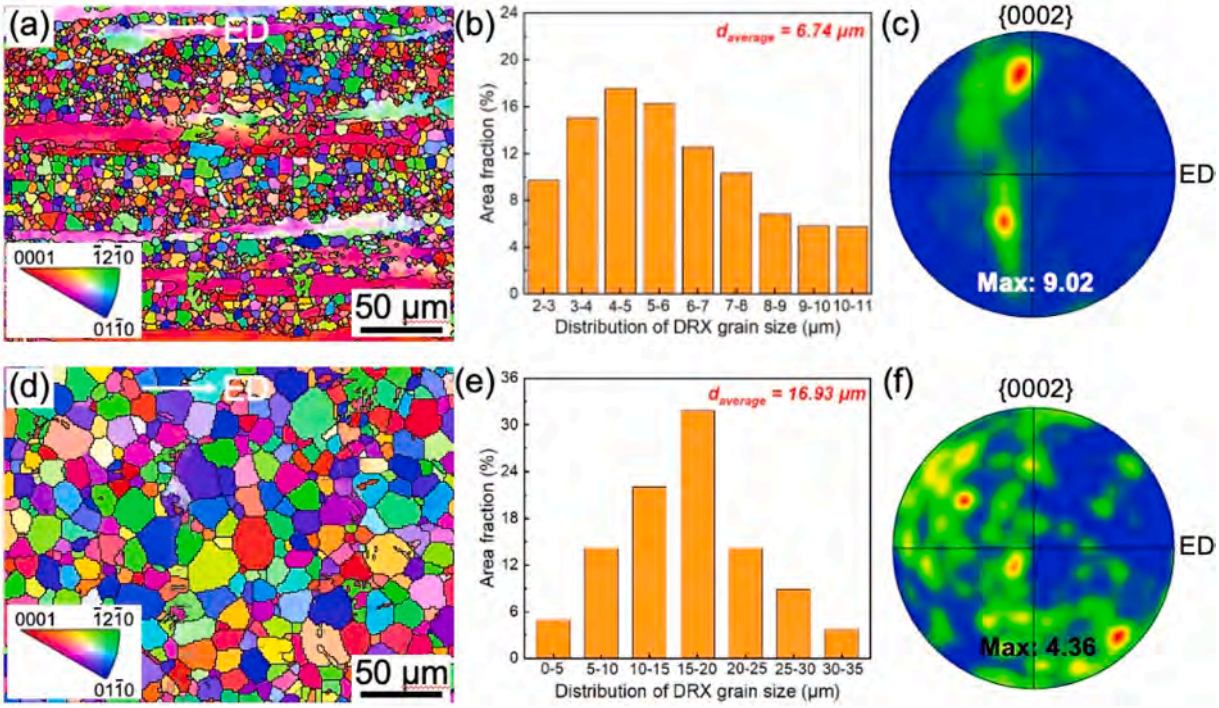

Fig. 3. IPF images, DRXed grain size distributions, and PF images: (a-c) WA61–400-E and (d-f) WA61–500-E.

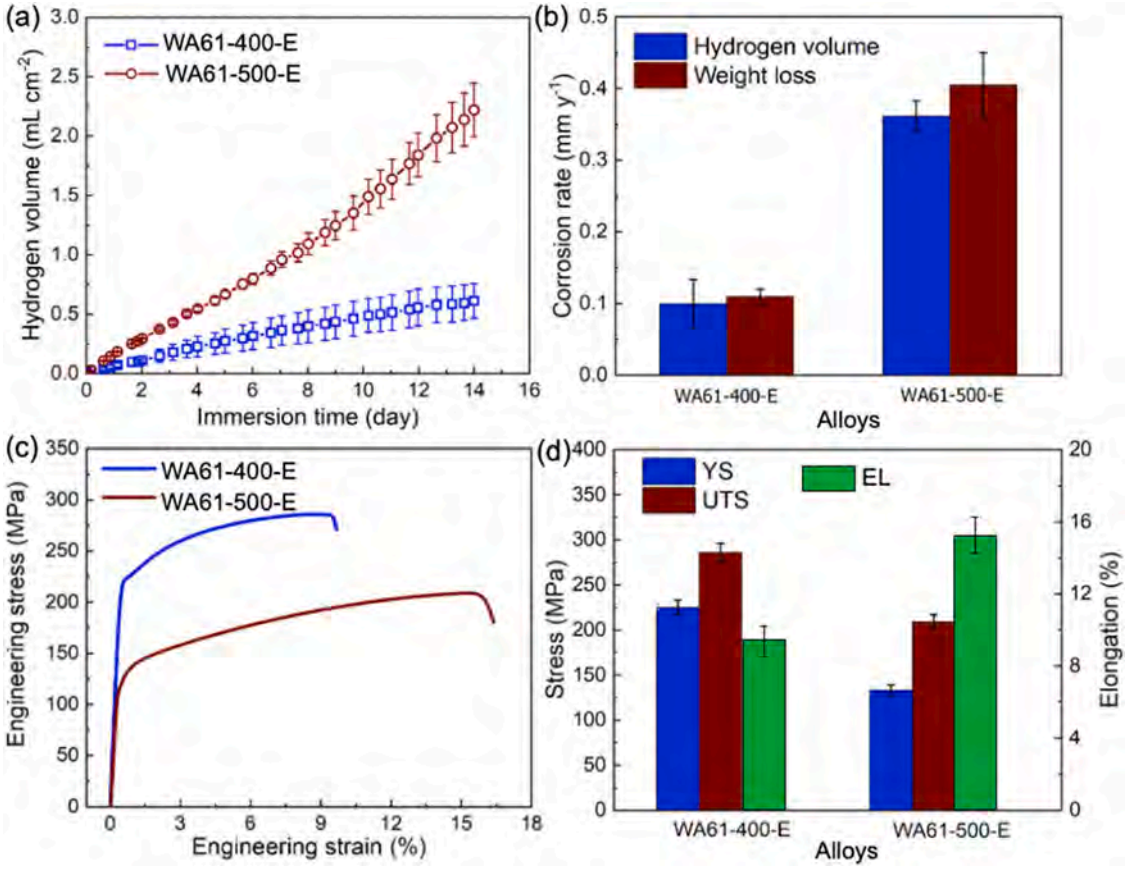

Fig. 4. Corrosion and mechanical properties of WA61–400-E containing the LPSO phase and WA61–500-E alloy without the LPSO phase: (a) Volume of hydrogen evolved as a function of time during immersion in a 3.5 wt% NaCl solution; (b) Average corrosion rates determined by the hydrogen volume and weight loss after immersion for 14 days; (c) Tensile stress-strain curves; (d) YS, UTS and elongations.

These results clearly indicate that the LPSO phases contribute to DRX grain refinement. The {0001} PFs along the extrusion direction (ED) of WA61–400-E and WA61–500-E are shown in Fig. 3c and f, which reveal that the maximum basal texture intensities of the DRXed grains in the α-Mg matrix are 9.02 and 4.36 mrd, respectively. The formation of LPSO phases consumes Y from the α-Mg matrix in WA61–400-E, consequently reducing the availability of Y. This is known to facilitate the activation of non-basal slip systems during hot extrusion and increase the basal texture intensity compared to WA61–500-E [32].

3.2. Corrosion and mechanical properties

Fig. 4a and b present the corrosion rates determined by hydrogen evolution and weight losses after 14-day immersion in the 3.5 wt% NaCl solution. The WA61–500-E alloy with a coarser grain size exhibits rapid and sustained hydrogen evolution, showing average corrosion rates of 0.36 mm y^{-1} based on hydrogen evolution and 0.41 mm y^{-1} based on mass loss. Conversely, WA61–400-E with a refined grain structure due to the LPSO phase shows significantly slower corrosion kinetics, as reflected by reduced hydrogen evolution and smaller corrosion rates of 0.10 mm y^{-1} (based on hydrogen evolution) and 0.11 mm y^{-1} (from mass loss). These results show that grain refinement achieved by the incorporation of the LPSO phase enhances the corrosion resistance in the chloride medium.

The tensile stress-strain curves and corresponding YS, UTS, and elongations (EL) of WA61–400-E and WA61–500-E are presented in Fig. 4c and d. The WA61–500-E alloy with a coarse grain size exhibits a YS of 133 ± 6 MPa, UTS of 209 ± 8 MPa and EL of 15.5 ± 8 %. After introducing the LPSO phase and reducing the grain size, significant improvements in both YS and UTS are observed, although elongation decreases. Specifically, WA61–400-E shows a YS of 225 ± 8 MPa, UTS of 286 ± 10 MPa, and EL of 9.4 ± 1.3 %.

Fig. 5 compares the UTS and average corrosion rates of the WA61–400-E and WA61–500-E alloys with those of common Mg alloys [33–42]. Conventional Mg-Al, Mg-Zn, Mg-Sn, Mg-RE, and Mg-RE-Zn alloys generally exhibit either high corrosion rates or limited mechanical strength. For instance, high-strength Mg-RE-Zn alloys have poor corrosion resistance, with corrosion rates ranging from approximately 1 to 60 mm y^{-1} , primarily due to galvanic coupling and coarse secondary phases. In contrast, WA61–400-E shows a better balance, as manifested by an elevated UTS of 300 MPa and a low corrosion rate of 0.1 mm y^{-1}.

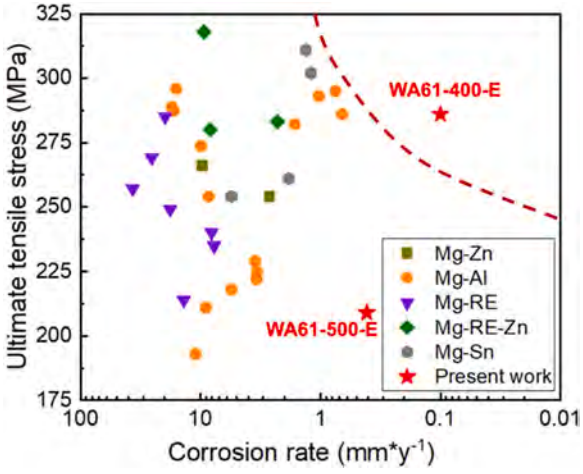

Fig. 5. The UTS-corrosion rate map comparing WA61–400-E and WA61–500-E (this work) with representative Mg-based alloys: Mg-Al [33–35], Mg-Zn [36, 37], Mg-Sn [38], Mg-RE [39–41], and Mg-RE-Zn [39,42]. Corrosion rates were obtained from immersion tests in 3.5 wt% NaCl solution.

3.3. Electrochemical measurements

Fig. 6 displays the potentiodynamic polarization curves of WA61–400-E and WA61–500-E in 3.5 wt% NaCl at 25 ± 1°C for different durations. The corrosion parameters, including the corrosion potential (E_{corr}), corrosion current density (I_{corr}), and breakdown potential (E_b) determined by cathodic Tafel extrapolation, are summarized in Table 2. Typically, the anodic polarization branch corresponds to metal dissolution, while the cathodic branch reflects hydrogen evolution [2,43–46]. After immersion for 0.5 h (Fig. 6a), WA61–400-E exhibits a more noble E_{corr} than WA61–500-E. The I_{corr} of WA61–400-E is estimated to be 58.9 μA cm^{-2}, which is close to that of WA61–500-E (62.1 μA cm^{-2}). After long immersion (72 h, Fig. 6b), WA61–400-E shows a distinct passivation behavior with a clear breakdown potential (E_b) at −1.36 V_{SCE}, indicating the formation of a protective film. Conversely, WA61–500-E does not exhibit an evident passivation behavior by retaining lower E_{corr} and higher corrosion current density. Cathodic analysis indicates significant differences, with WA61–400-E showing an I_{corr} of 2.23 μA cm^{-2} compared to 95.3 μA cm^{-2} for WA61–500-E. The trends are consistent with those observed from hydrogen evolution (Fig. 4a).

The EIS plots of WA61–400-E and WA61–500-E after immersion for 0.5 h, 6 h, 24 h, and 72 h are depicted in Fig. 7. The corresponding equivalent circuits used for fitting the EIS spectra are shown in the insets, and the fitting parameters are summarized in Table 3. In the equivalent circuits, R_s represents the solution resistance, R_{ct} and CPE_{dl} correspond to the charge transfer resistance and electric double-layer capacitance, respectively, R_f and CPE_f denote the resistance and capacitance of the surface film, and the inductance L in series with resistance R_L accounts for localized breakdown of the protective film due to Mg^{2+} reaction[43,47,48]. During initial immersion (0.5 h), both alloys exhibit two characteristic loops in the EIS spectra: a high-frequency capacitive loop and a medium-frequency capacitive loop. As the immersion time goes up from 6 h to 72 h, WA61–400-E retains two loops, and the loop diameters expand progressively with immersion time. Correspondingly, R_f increases from 1656 to 5848 Ω cm^2 after the immersion time is increased from 0.5 h to 72 h (Table 3), indicating the gradual development of a protective passive layer. In contrast, the EIS plots of WA61–500-E display three loops at longer immersion time (Fig. 7c–d). After immersion for 6 h, the inductive component (L) in series with R_f suggests the onset of corrosion film degradation. The deterioration of the protective film increases the corrosion rate due to the ineffective barrier against chloride attack.

3.4. Corrosion morphology and product

Fig. 8 shows the corrosion morphology of WA61–400-E and WA61–500-E alloys after immersion in 3.5 wt% NaCl for 1 h. WA61–400-E (Fig. 8a) exhibits a relatively compact corrosion morphology, characterized by a smooth surface with limited local pitting. Fig. 8b and c further reveal that the corrosion film on the alloy is dense and continuous, boding well for corrosion protection. In contrast, WA61–500-E displays a heterogeneous corrosion morphology and local pitting (Fig. 8d and e). The magnified image of the non-pitting area (Fig. 8f) reveals a less compact corrosion film compared to that on WA61–400-E (Fig. 8c) and inferior corrosion resistance.

To further assess the spatial evolution of corrosion, the 3D CLSM images acquired after immersion for 3 days are shown in Fig. 9. The corrosion products on WA61–400-E (Fig. 9a) exhibit a relatively smooth surface with minimal height variation. After removal of the corrosion products (Fig. 9b), the surface remains largely uniform, indicating that corrosion occurs in a general and shallow manner. In contrast, the WA61–500-E sample exhibits pronounced surface heterogeneity, characterized by the formation of large and deep corrosion pits (Fig. 9c and d). Notably, Regions A and B in Fig. 9d reveal typical pits with widths of approximately 27 μm and 37 μm, and depths of 16 μm and 18 μm,

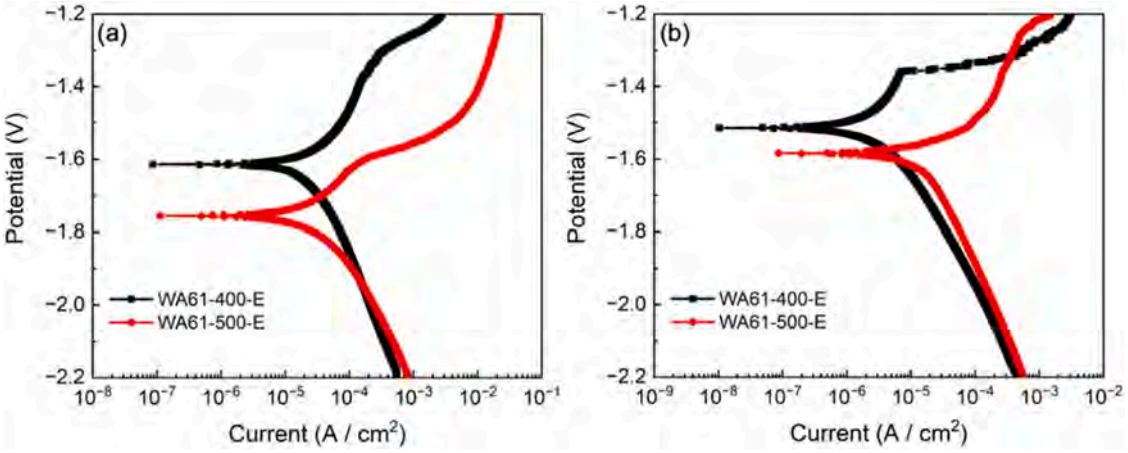

Fig. 6. Polarization curves of WA61–400-E and WA61–500-E immersed in 3.5 wt% NaCl for (a) 0.5 h and (b) 72 h.

Table 2
Fitted results from the polarization curves of WA61-400-E and WA61-500-E.

Alloys	Immersion time	E_{corr} (V_{SCE})	I_{corr} (μA cm^{-2})	E_b (V_{SCE})
WA61–400-E	0.5 h	−1.61	58.9	–
	72 h	−1.51	2.23	−1.36
WA61–500-E	0.5 h	−1.76	62.1	–
	72 h	−1.58	95.3	–

respectively. Throughout the immersion period from 1 h to 3 days, WA61–400-E consistently demonstrates a uniform corrosion mode, whereas WA61–500-E undergoes progressively intensified pitting corrosion, marked by increased pit density and depth. This trend is consistent with that observed from hydrogen evolution and weight loss measurements (Fig. 4a).

Fig. 10 presents the macroscopic and microscopic surface morphologies of WA61–400-E and WA61–500-E after immersion for 14 days in 3.5 wt% NaCl. WA61–400-E maintains a relatively smooth surface with minimal visible damage (Fig. 10a), whereas the WA61–500-E alloy exhibits pronounced corrosion pits across the surface (Fig. 10b).

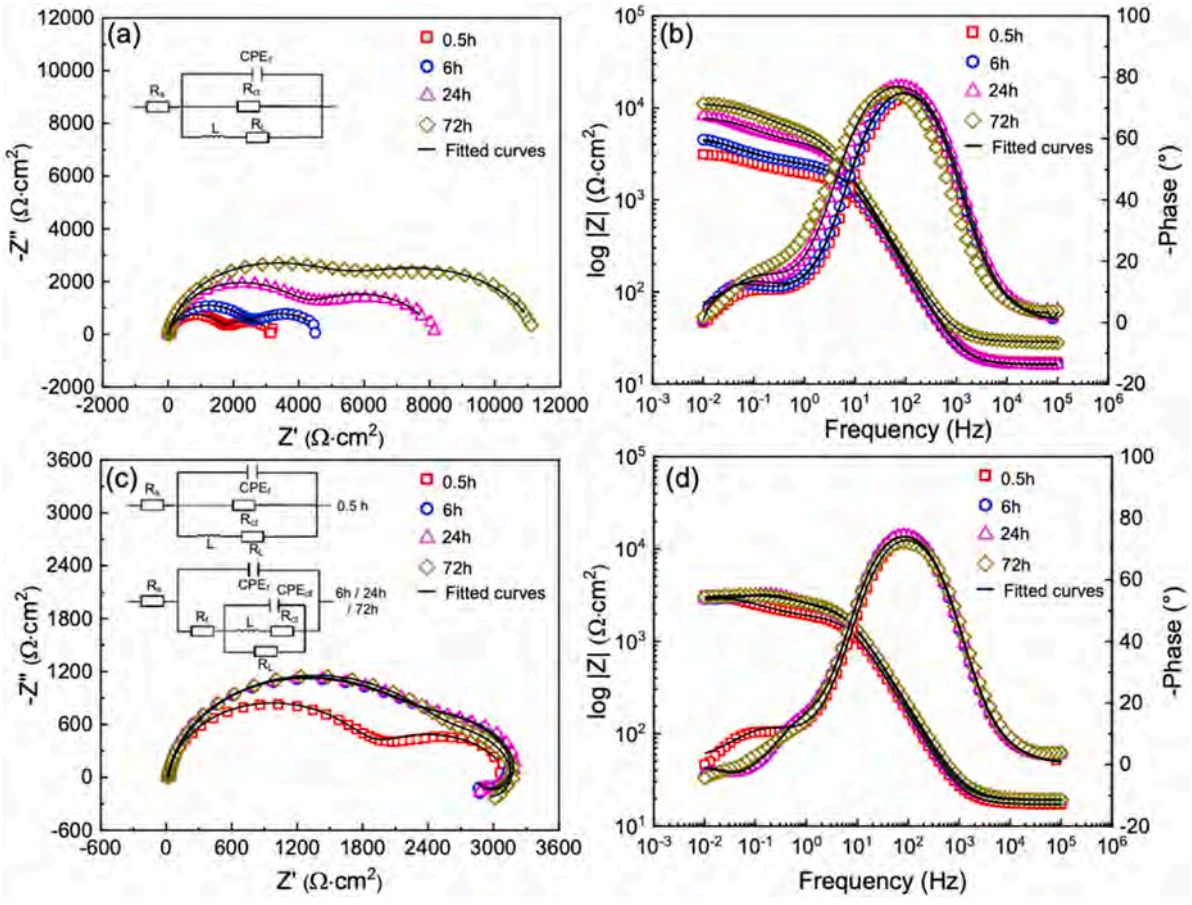

Fig. 7. Nyquist and Bode plots after immersion for 0.5 h, 6 h, 24 h, and 72 h: (a, b) WA61–400-E and (c, d) WA61–500-E.

Table 3
Fitted results based on EIS plots of WA61-400-E and WA61-500-E.

Alloys	Immersion time (h)	R_s (Ω cm^2)	R_{ct} (Ω cm^2)	CPE_{dl}		R_f (Ω cm^2)	CPE_f		R_L (Ω cm^2)	L (H cm^{-2})
				(Ω^{-1}s^n cm^{-2})	n_{dl}		(Ω^{-1} s^n cm^{-2})	n_f		
WA61–400-E	0.5	17	1523	0.001	0.72	1656	1.4E−5	0.93	/	/
	6	16	2284	0.001	0.72	2398	1.4E−5	0.93	/	/
	24	16	3879	0.0005	0.76	4286	1.3E−5	0.93	/	/
	72	18	5430	0.0002	0.78	5848	1.3E−5	0.92	/	/
WA61–500-E	0.5	17	1269	0.001	0.75	1869	1.5E−5	0.93	/	/
	6	19	662	0.0004	0.96	2482	1.3E−5	0.93	710	3841
	24	19	561	0.0004	0.97	2509	1.3E−5	0.93	709	3739
	72	19	11	0.0008	0.99	2670	1.5E−5	0.91	479	9042

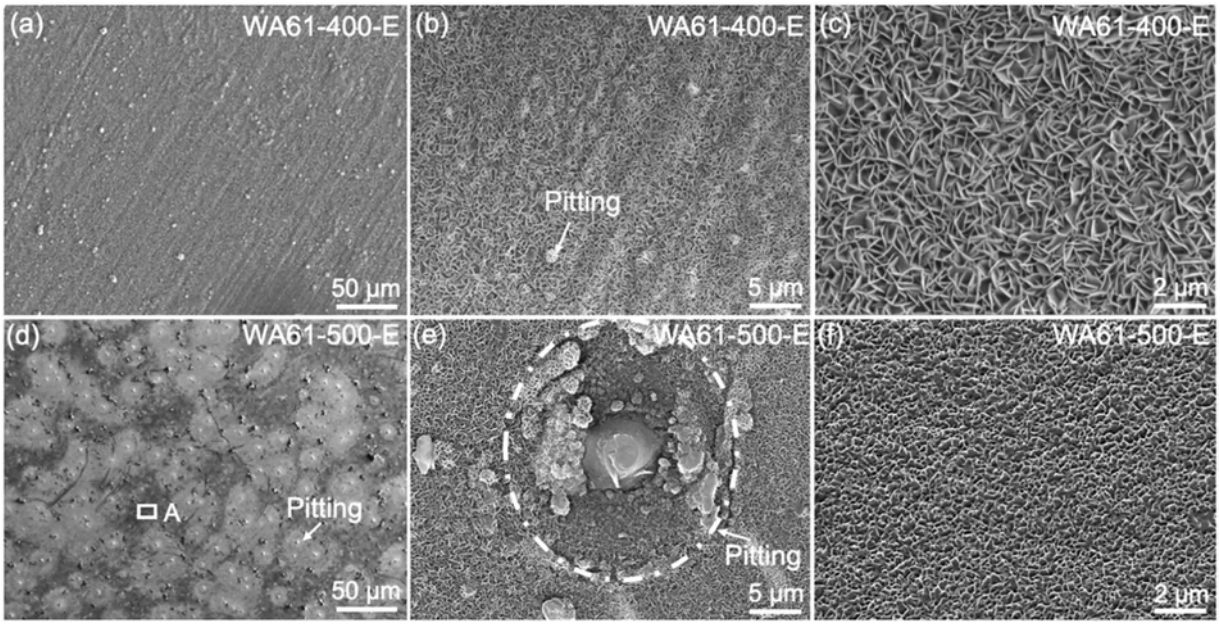

Fig. 8. SEM surface morphologies after immersion in 3.5 wt% NaCl solution for 1 h: (a-c) WA61–400-E and (d-f) WA61–500-E.

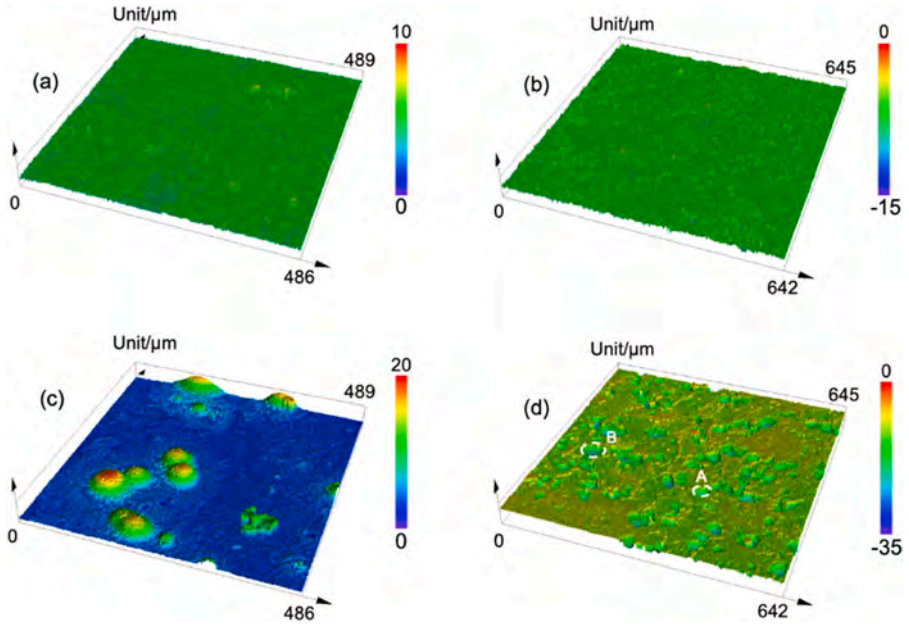

Fig. 9. 3D CLSM images after immersion for 3 days: (a) WA61–400-E with corrosion products; (b) WA61–400-E after removing corrosion products; (c) WA61–500-E alloy with corrosion products; (d) WA61–500-E after removing corrosion products.

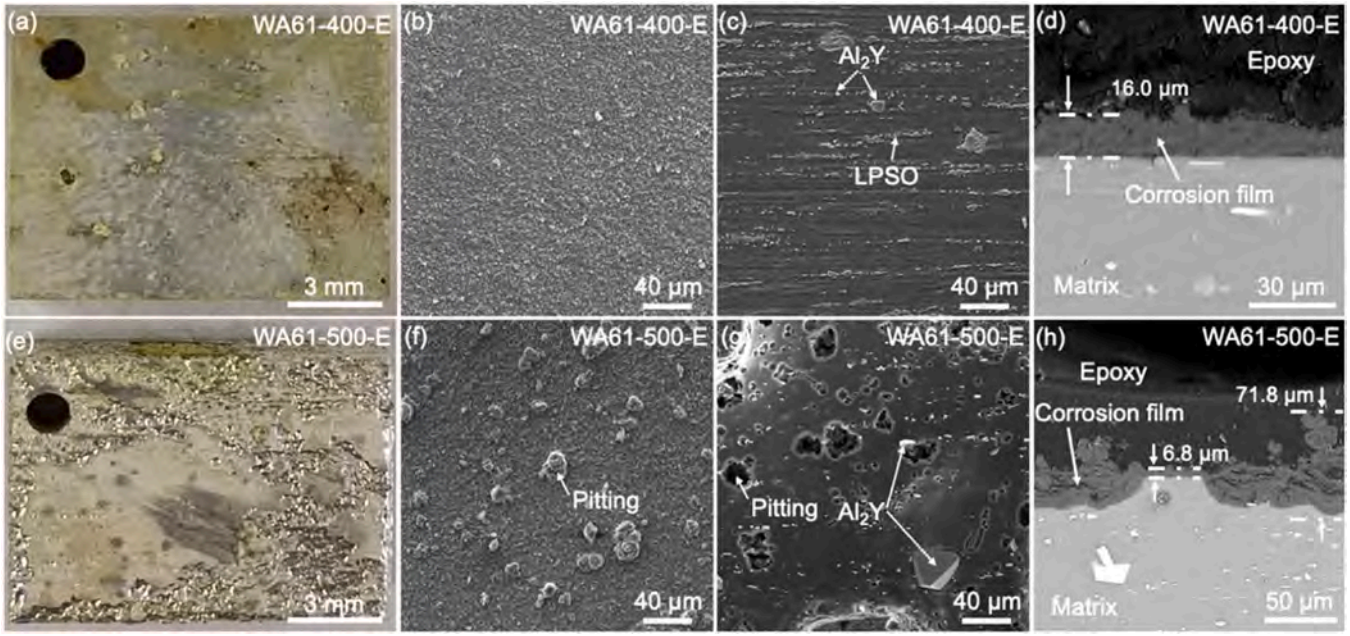

Fig. 10. SEM surface and cross-sectional morphologies after immersion in 3.5 wt% NaCl for 14 days: (a-d) WA61–400-E and (e-h) WA61–500-E.

WA61–400-E alloy shows a relatively uniform corrosion process before and after corrosion products are removed (Fig. 10c and d). The cross-sectional image shows the formation of a dense and continuous corrosion film with a thickness of 16 μm, a flat and well-defined interface, and effective protection of the underlying substrate. In contrast, WA61–500-E exhibits severe localized pitting corrosion (Fig. 10f and g). The associated corrosion film is non-uniform, loose, and variable in thickness, ranging from 16 μm to 71.8 μm. This degraded film compromises the protective capability, leading to significantly higher corrosion rates on WA61–500-E than WA61–400-E. The superior corrosion resistance of WA61–400-E is primarily attributed to the formation of a more continuous and protective corrosion product film.

To determine the composition of the corrosion product films, XPS is conducted on WA61–400-E and WA61–500-E after immersion for 12 h. The Mg 1 *s* spectra display two distinct peaks at 1303.9 eV and 1302.7 eV corresponding to MgO and $Mg(OH)_2$, respectively (Fig. 11a for WA-400-E and Fig. 11d for WA61–500-E). There is a clear peak at 73.62 eV indicative of Al_2O_3. The corrosion products on both alloys primarily consist of MgO, $Mg(OH)_2$, Y_2O_3, and Al_2O_3. Interestingly, WA61–400-E shows a more intense $Mg(OH)_2$ peak than WA61–500-E,

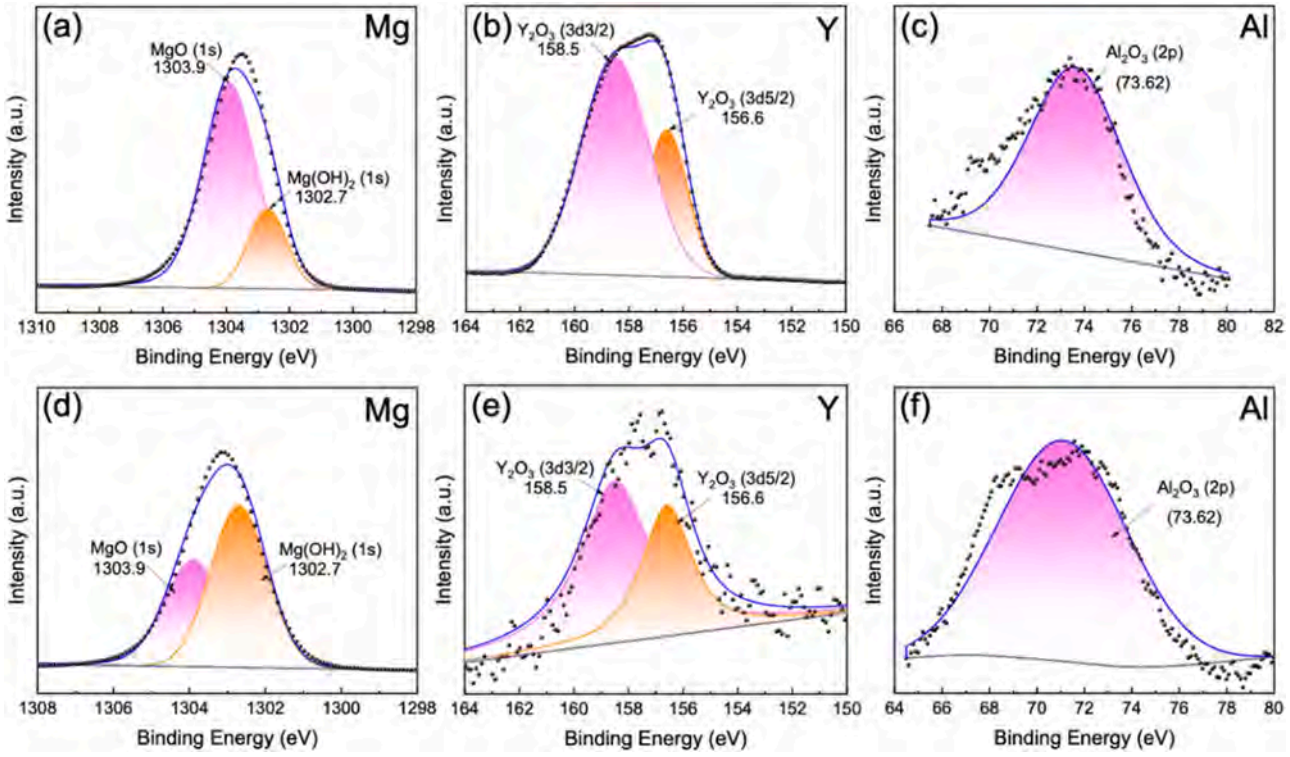

Fig. 11. XPS spectra of the corrosion product films after immersion in 3.5 wt% NaCl for 12 h: (a-c) WA61–400-E and (d-f) WA61–500-E.

suggesting a larger quantity of corrosion products and a denser, more complete, and protective corrosion film.

4. Discussion

The LPSO phase plays an important role in the microstructure, mechanical properties, and corrosion resistance of Mg alloys [49,50]. In this study, the precipitation of the LPSO phase in the WA61 alloy can be tailored precisely by adjusting the pre-extrusion heat treatment temperature. At 400 ℃, abundant LPSO phases are formed, while a higher temperature of 500 ℃ suppresses their formation (Fig. 1). The results agree well with the CALPHAD-type calculations (Fig. 2) and enable a direct evaluation of the LPSO-related effects in Mg-Y-Al alloys.

The LPSO phase produces pronounced grain refinement by the PSN mechanisms and pinning DRX grain boundaries (Fig. 1d and e) and reduces the average grain size from 16.93 μm in WA61–500-E to 6.74 μm in WA61–400-E (Fig. 3). Grain refinement enhances YS by increasing the grain boundary area, thus impeding dislocation motion *via* the Hall-Petch (HP) effect. Wen et al. [6] have reported that the HP coefficient is approximately 220 MPa*$\mu m^{1/2}$ for the Mg-Y based alloys, indicating that the grain refinement strengthening is strong in Mg-Y-Al alloys. In addition, B-LPSO and N-LPSO align along the extrusion direction to provide short-fiber reinforcement for effective bearing of applied loads and blocking dislocation glide [51]. Based on previous results, a 1 % $V_{(LPSO)}$ phase can provide a strength increment of 13–15 MPa in Mg-Y-Al alloys, which is consistent with the strength improvement of WA61–400-E [15]. However, despite these benefits, the LPSO phase generally gives rise to reduced ductility, due to the relatively brittle nature and its tendency to promote strain localization [28,52]. However, WA61–400-E with the LPSO phase exhibits the desirable strength-ductility synergy on account of the solution of Y atoms in the α-Mg matrix. Sandlöbes and Huang et al. [53,54] have shown that Y can lower the CRSS ratios between non-basal and basal slip systems to activate multiple slip systems and promote uniform plastic deformation. As a result, the local stress concentrations in the LPSO phase are relieved to mitigate premature failure.

The LPSO phase can act as a micro-cathode relative to the α-Mg matrix, resulting in micro-galvanic corrosion and accelerated corrosion in most Mg alloys [26]. The LPSO phase, which typically contains higher concentrations of rare earth and transition metal elements, exhibits a more noble surface potential than the surrounding Mg matrix. Upon exposure to a corrosive environment, galvanic coupling is established at the interface between the LPSO phase and the α-Mg matrix [26]. Although the LPSO phase promotes micro-galvanic corrosion and accelerates local dissolution, it is surprising to find that the corrosion resistance is improved after the introduction of the LPSO phase to WA61–400-E, with a corrosion rate of 0.1 mm y^{-1} that is lower than 0.36 mm y^{-1} of WA61–500-E without the LPSO phase (Fig. 4). This improvement arises from the unique chemistry of the Mg-Y-Al system and the modulated microstructure.

Mg-Y-Al alloys form a compact corrosion film largely due to the rapid deposition of Al^{3+} and Y^{3+} in the initial corrosion stage [29]. The self-passivating corrosion film shields the Mg substrate from the corrosive environment and renders it insensitive to micro-galvanic corrosion of the LPSO phase. The protection by corrosion film formation is related to the microstructure. Compared to WA61–500-E, grain refinement of WA61–400-E accelerates nucleation and growth of compact, continuous corrosion films by increasing the density of grain boundaries (Fig. 8a-c). This corrosion product film can provide long-term protection (Fig. 10a-c). However, WA61–500-E has coarse grains that are more vulnerable to local attack, as shown in Fig. 8d-f (1 h), Fig. 9c-d (3 days), and Fig. 10d-f (14 days). The protection by the corrosion product film decreases compared to WA61–400-E (Figs. 6 and 7). In fact, grain refinement can accelerate the nucleation and growth of compact, continuous corrosion product films by increasing the density of grain boundaries, which serve as rapid diffusion paths for film-forming ions [9,43,55]. Fig. 12 compares the structure and composition after immersion for 2 s in 3.5 wt% NaCl. The corrosion product films on WA61–400-E and WA61–500-E are composed of $Mg(OH)_2$ and MgO in line with XPS (Fig. 11). However, the average grain size of the corrosion film on WA61–400-E is 7 ± 2 nm, which is smaller than 12 ± 2 nm on WA61–500-E. The small size relieves the stress between the corrosion layer and matrix, consequently decreasing the cracking of the protective layer. Therefore, grain refinement of WA61 alloys mitigates pitting corrosion by reducing pit formation and promoting compact film coverage.

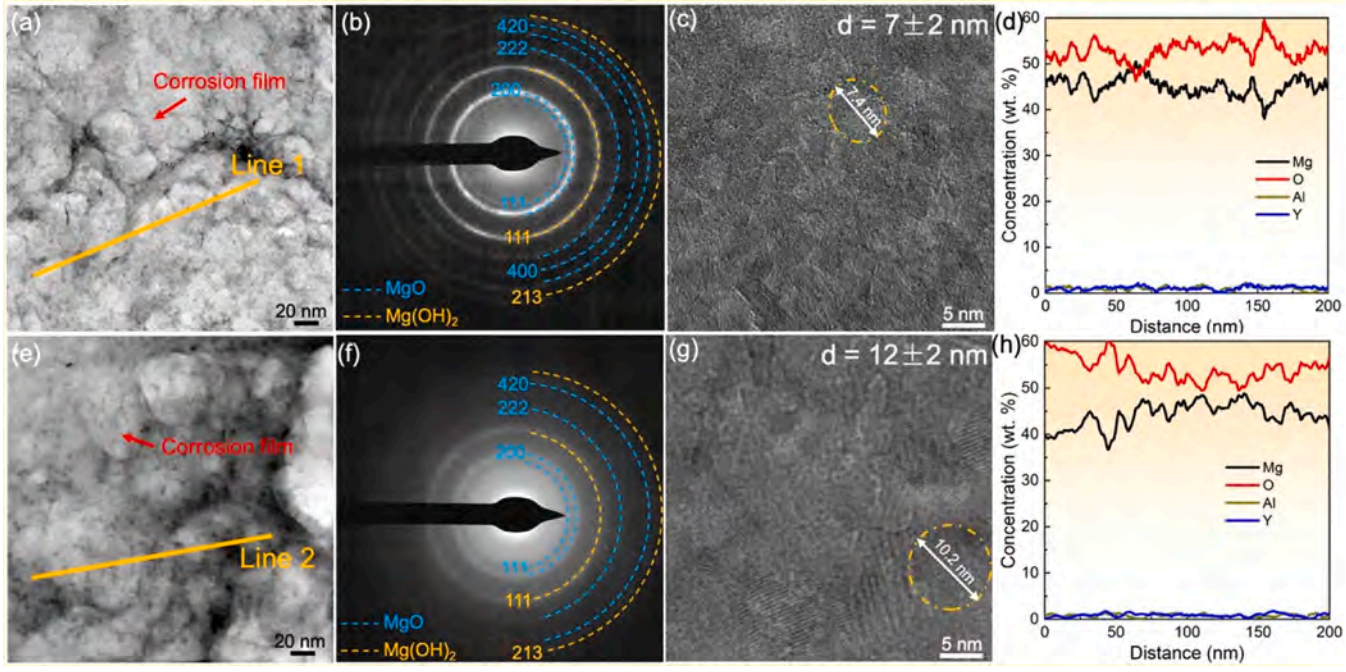

Fig. 12. TEM characterization of the thin foil after immersion for 2 s in 3.5 wt% NaCl: (a-d) BF images without precipitates in WA61–400-E, SAED patterns, HR-TEM images, and EDS line scans; (e-h) BF image without precipitates in WA61–500-E and SAED patterns, HR-TEM image, and EDS line scans.

Another factor that lowers the corrosion rate is the suppression of Al_2Y formation in WA61–400-E due to the competitive precipitation of the LPSO phase. The PD between the LPSO phase and α-Mg matrix in WA61–400-E alloy was measured by SKPFM, as shown in Fig. 13. The LPSO phase area is brighter than matrix, meaning that the LPSO phase has a more positive potential than the α-Mg matrix (Fig. 13a). In addition, the potential line profile analysis shows that the PD between LPSO phase and α-Mg matrix is about ~90 mV (Fig. 13b), which is comparable to those Mg alloys containing LPSO phase, such as ~90 mV in Mg-Gd-Zn [56,57], ~80 mV in Mg-Er-Zn-Zr alloy [56]. In comparison with LPSO phase, the Al_2Y particles have a significantly higher surface potential (~280 mV relative to α-Mg) than the LPSO relative to α-Mg, as shown in Fig. 13c and d. This large potential difference promotes micro-galvanic coupling and accelerates local corrosion where Al_2Y is present. By favoring LPSO formation and limiting Al_2Y precipitation, WA61–400-E suppresses galvanic interactions and pitting and improves the corrosion resistance compared to WA61–500-E, where Al_2Y is more abundant.

The corrosion mechanisms of WA61–400-E and WA61–500-E are illustrated schematically in Fig. 14. The superior corrosion resistance of the extruded Mg-Y-Al alloy containing the LPSO phase precipitate arises from three synergistic effects: (i) rapid formation of dense, self-passivating corrosion films driven by fast Al^{3+} and Y^{3+} deposition, with the LPSO phase minimizing micro-galvanic Al_2Y particles; (ii) pronounced grain refinement due to LPSO precipitation, which promotes compact and continuous protective layer formation (iii) suppression of Al_2Y phase formation by the LPSO phase, thereby reducing detrimental galvanic interactions and local pitting. Although the elongated LPSO lamellae increase the α-Mg/LPSO interfacial length, SKPFM shows a moderate PD for LPSO vs α-Mg, markedly lower than that of Al_2Y vs α-Mg. The galvanic driving force per unit interface is weaker for LPSO, whereas sparse Al_2Y particles act as strong local cathodes that preferentially initiate film disruption. Collectively, these factors enable WA61–400-E to achieve outstanding corrosion resistance and significantly outperform WA61–500-E in the aggressive chloride environment.

5. Conclusions

The intrinsic tradeoff between strength and corrosion resistance in Mg alloys is a technical challenge. In this study, a novel extruded WA61 alloy with the LPSO phase tailored by pre-extrusion heat treatment is fabricated. Introduction of the LPSO phase enhances the strength and corrosion resistance of the extruded WA61 alloy. The WA61–400-E alloy, with an average grain size of 6.74 μm and 7 % LPSO phase, exhibits a much higher yield strength (225 ± 8 MPa) and lower corrosion rate (0.10 $mm{\cdot}y^{-1}$ in 3.5 wt% NaCl) than the WA61–500-E alloy. The latter lacking the LPSO phase has a coarser grain size (16.93 μm), a lower yield strength (133 ± 6 MPa), and a higher corrosion rate (0.36 $mm{\cdot}y^{-1}$). The formation of a quasi-passivating, compact corrosion product film is responsible for the excellent long-term corrosion resistance of the LPSO-containing WA61–400-E alloy. In contrast, the WA61–500-E alloy with coarser grains and higher Al_2Y phase contents fails to develop such protective films and shows severe pitting and rapid corrosion. The corrosion resistance is substantially enhanced by the precipitation of the LPSO phase, which promotes grain refinement and suppresses the formation of the Al_2Y phase. This dual effect accelerates the nucleation and growth of a compact, continuous corrosion product film and inhibits pit initiation. The LPSO phase leads to concurrent improvement in both the strength and corrosion resistance of Mg-Y-Al alloys. The results reveal a new strategy to develop Mg alloys with superior durability and structural properties.

CRediT authorship contribution statement

Xiaoqin Zeng: Writing – review & editing, Supervision. **Paul K.**

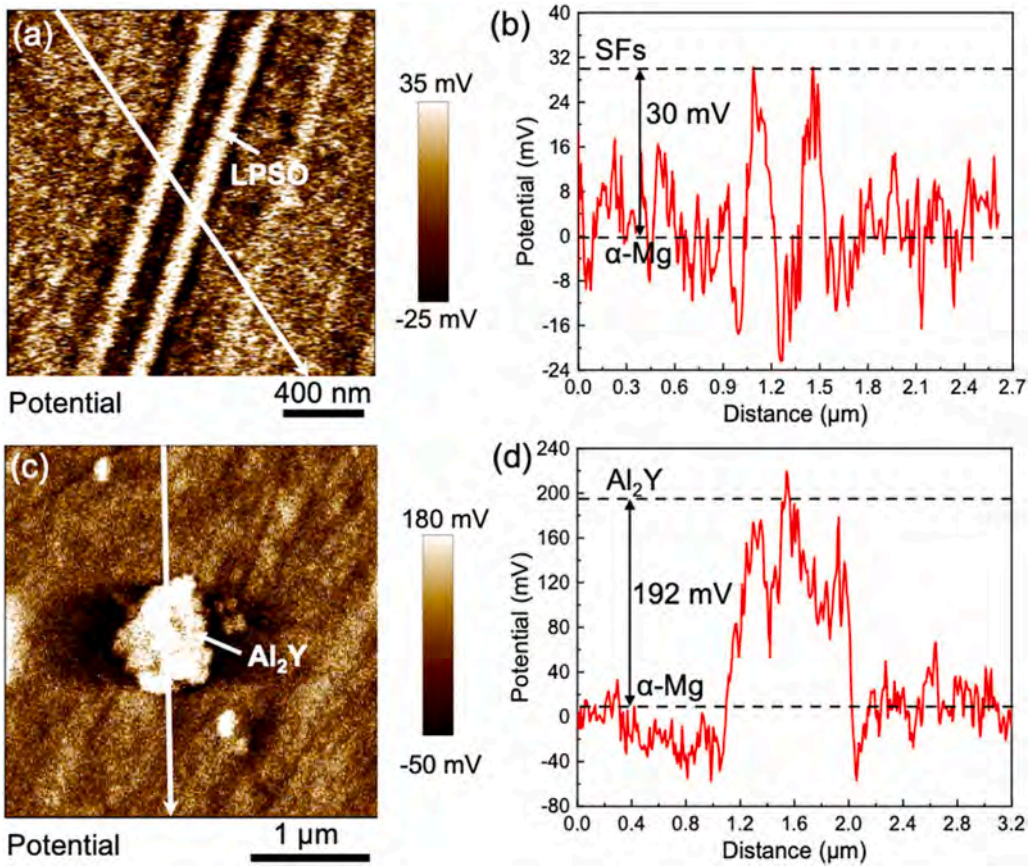

Fig. 13. Surface potential maps and corresponding Volta potential profiles of secondary phases in WA61–400-E alloy: (a, b) LPSO phase and (c, d) Al_2Y phase.

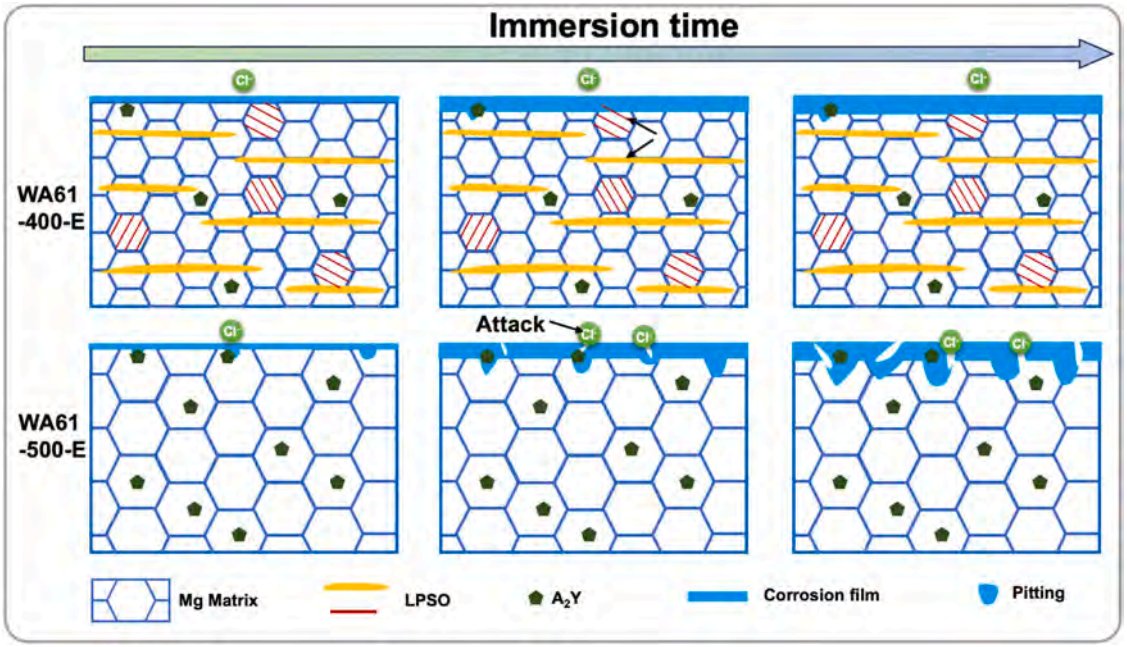

Fig. 14. Schematic diagram showing the corrosion mechanism of WA61–400-E and WA61–500-E.

Chu: Writing – review & editing, Formal analysis. **Chao Yang:** Writing – review & editing, Methodology. **Jie Wang:** Supervision. **Chao Wu:** Writing – review & editing. **Yuyang Chen:** Writing – review & editing, Project administration, Conceptualization. **Yiwen Chen:** Writing – review & editing, Writing – original draft, Methodology, Funding acquisition, Data curation, Conceptualization.

Declaration of Competing Interest

The authors declare that they have no conflicts of interest related to this submission. On behalf of all co-authors, I confirm that this manuscript is original, has not been published previously, and is not under consideration for publication elsewhere, either in whole or in part. All authors have reviewed and approved the final version of the manuscript for submission.

Acknowledgments

This work was supported by the Fundamental Research Funds for the Central Universities (JUSRP202501073), Wuxi Science and Technology Development Fund Project (K20241040), National Natural Science Foundation of China (No. 52401101, 52204372, 52501155), Natural Science Foundation of Jiangsu Province (No. BK20250406899), Postdoctoral Fellowship Program of CPSF under Grant Number GZC20231545, China Postdoctoral Science Foundation (2024T170557 and 2023M742224), Shanghai Post-doctoral Excellence Program (No. 2023440), City University of Hong Kong Donation Research Grants (DON-RMG 9229021 and 9220061), as well as Guangdong - Hong Kong Technology Cooperation Funding Scheme (TCFS GHP/212/22GD and CityU 9440399).

References

[1] J.F. Nie, K.S. Shin, Z.R. Zeng, Metall. Mater. Trans. A 51 (12) (2020) 6045–6109.
[2] X. Hao, Y. Hu, Y. Zhen, Y. Wen, L. Peng, Q. Xu, Y. Hou, P. Zhou, J. Xiao, X. Wang, Corros. Commun. (2025).
[3] H. Liu, H. Huang, C. Wang, J. Sun, J. Bai, F. Xue, A. Ma, X.-B. Chen, Jom 71 (9) (2019) 3314–3327.
[4] P. Zhou, C. Li, G. Jiao, T. Lv, T. Zhang, F. Wang, J. Mater. Sci. Technol. 216 (2025) 66–80.
[5] Y. Zhen, C. Lin, Y. Hu, Z. Ren, P. Zhou, B. Dou, J. Xiao, J. Sun, X. Wang, Y. Yuan, Corros. Commun. 15 (2024) 24–35.
[6] Y. Wen, B. Guan, Y. Xin, C. Liu, P. Wu, G. Huang, Q. Liu, Scr. Mater. 210 (2022) 114451.
[7] R. Zheng, W. Gong, J.-p Du, S. Gao, M. Liu, G. Li, T. Kawasaki, S. Harjo, C. Ma, S. Ogata, N. Tsuji, Acta Mater. 238 (2022) 118243.
[8] C. Yan, Y. Xin, X.B. Chen, D. Xu, P.K. Chu, C. Liu, B. Guan, X. Huang, Q. Liu, Nat. Commun. 12 (1) (2021) 4616.
[9] N.N. Aung, W. Zhou, Corros. Sci. 52 (2) (2010) 589–594.
[10] X. Heng, Y. Zhang, W. Rong, Y. Wu, L. Peng, Mater. Des. 169 (2019) 107666.
[11] X.-j Zhou, C.-m Liu, Y.-h Gao, S.-n Jiang, X.-z Han, Z.-y Chen, Metall. Mater. Trans. A 48 (6) (2017) 3060–3072.
[12] D. Zhang, Z. Tan, Q. Huo, Z. Xiao, Z. Fang, X. Yang, Mater. Sci. Eng. A 715 (2018) 389–403.
[13] Y. Jono, M. Yamasaki, Y. Kawamura, Mater. Trans. 54 (5) (2013) 703–712.
[14] Y. Chen, M. Yu, J. Wang, Q. Li, W. Zheng, J. Li, X. Zeng, Mater. Des. 235 (2023) 112400.
[15] Y. Chen, J. Wang, W. Zheng, Q. Li, M. Yu, T. Ying, X. Zeng, Acta Mater. 263 (2024) 119521.
[16] D. Qiu, M.X. Zhang, J.A. Taylor, P.M. Kelly, Acta Mater. 57 (10) (2009) 3052–3059.
[17] Y.X. Li, D. Qiu, Y.H. Rong, M.X. Zhang, Philos. Mag. 94 (12) (2014) 1311–1326.
[18] F. Khorasani, M. Emamy, M. Malekan, H. Mirzadeh, B. Pourbahari, T. Krajnák, P. Minárik, Mater. Charact. 147 (2019) 155–164.
[19] Y.-K. Li, M. Zha, H.-L. Jia, S.-Q. Wang, H.-M. Zhang, X. Ma, T. Tian, P.-K. Ma, H.-Y. Wang, J. Magnes. Alloy 9 (5) (2021) 1556–1566.
[20] K. Hagihara, A. Kinoshita, Y. Sugino, M. Yamasaki, Y. Kawamura, H.Y. Yasuda, Y. Umakoshi, Acta Mater. 58 (19) (2010) 6282–6293.
[21] C. Liu, Q. Luo, Q.-F. Gu, Q. Li, K.-C. Chou, J. Magnes, Alloy (2021).
[22] J. Shao, Z. Chen, T. Chen, Z. Hu, X. Zhou, C. Liu, J. Magnes. Alloy 4 (2) (2016) 83–88.
[23] J. Li, F. Wang, J. Zeng, C. Zhao, L. Jin, J. Dong, Mater. Charact. 193 (2022) 112326.
[24] M. Li, G. Zhang, S. Yin, C. Wang, Y. Fu, C. Gu, R. Guan, J. Magnes, Alloy (2022).
[25] J. Xie, J. Zhang, Z. Zhang, Z. Yu, Z. Xu, R. Wang, D. Fang, X. Zhang, X. Zhang, R. Wu, J. Mater. Sci. Technol. 151 (2023) 190–203.
[26] J. Zhang, J. Xu, W. Cheng, C. Chen, J. Kang, J. Mater. Sci. Technol. 28 (12) (2012) 1157–1162.
[27] C.Q. Li, D.K. Xu, Z.R. Zeng, B.J. Wang, L.Y. Sheng, X.B. Chen, E.H. Han, Mater. Des. 121 (2017) 430–441.
[28] X. Zhou, W. Xiong, G. Zeng, H. Xiao, J. Zhang, X. Lu, X. Chen, Mater. Sci. Eng. A 805 (2021) 140596.
[29] Q. Zhu, Y. Li, F. Cao, D. Qiu, Y. Yang, J. Wang, H. Zhang, T. Ying, W. Ding, X. Zeng, Nat. Commun. 13 (1) (2022) 5838.
[30] Y. Chen, T. Ying, Y. Yang, J. Wang, X. Zeng, Corros. Sci. 216 (2023) 111106.
[31] Y. Chen, Q. Li, Y. Li, Z. Weisen, W. Jingya, X. Zeng, J. Mater. Sci. Technol. 126 (2022) 80–92.
[32] W. Li, L. Wang, B. Zhou, C. Liu, X. Zeng, J. Mater. Sci. Technol. 35 (10) (2019) 2200–2206.
[33] Z. Zhang, J. Xie, J. Zhang, H. Dong, S. Liu, X. Zhang, J. Wang, R. Wu, J. Mater. Sci. Technol. 150 (2023) 49–64.
[34] B.-s Liu, H.-H. Wang, Y.-z Zhang, Y.-x Yang, X.-x Ren, H.-y Du, L.-f Hou, Y.-h Wei, G.-l Song, J. Phys. Chem. Solids 150 (2021) 109851.
[35] Y. Hu, C. Zhang, W. Meng, F. Pan, J. Zhou, J. Alloy Compd. 727 (2017) 491–500.

[36] B.J. Wang, D.K. Xu, J. Sun, E.-H. Han, Corros. Sci. 157 (2019) 347–356.
[37] S. Yin, W. Duan, W. Liu, L. Wu, J. Yu, Z. Zhao, M. Liu, P. Wang, J. Cui, Z. Zhang, Corros. Sci. 166 (2020) 108419.
[38] X. Wang, Z. Chen, E. Guo, X. Liu, H. Kang, T. Wang, J. Alloy Compd. 863 (2021).
[39] Y. Subasi, Y. Turen, H. Zengin, H. Ahlatci, Y. Sun, Mater. Res. Express 6 (11) (2019).
[40] J. Li, R. Chen, Y. Ma, W. Ke, J. Magnes. Alloy 1 (4) (2013) 346–351.
[41] Q. Jiang, X. Lv, D. Lu, J. Zhang, B. Hou, J. Magnes. Alloy 6 (4) (2018) 346–355.
[42] A. Srinivasan, Y. Huang, C.L. Mendis, C. Blawert, K.U. Kainer, N. Hort, Mater. Sci. Eng. A 595 (2014) 224–234.
[43] G.L. Song, A. Atrens, Adv. Eng. Mater. 1 (1) (1999) 11–33.
[44] A. Atrens, Z. Shi, S.U. Mehreen, S. Johnston, G.-L. Song, X. Chen, F. Pan, J. Magnes. Alloy 8 (4) (2020) 989–998.
[45] C. Yang, T. Ying, A. Huang, J. Huang, P. Chen, P.K. Chu, X. Zeng, Corros. Commun. 17 (2025) 35–43.
[46] P. Zhou, S. Sun, X. Liu, S. Meng, Z. Du, Z. Tang, D. Li, J. Sun, Y. Yuan, B. Tribollet, Corros. Sci. (2025) 112750.
[47] G.-L. Song, A. Atrens, J. Magnes. Alloy 11 (11) (2023) 3948–3991.
[48] Y. Chen, Q. Wang, L. Hou, H. Huang, Z. Gao, Y. Wei, Exploration (2025).
[49] G. Wu, C. Wang, M. Sun, W. Ding, J. Magnes. Alloy 9 (1) (2021) 1–20.
[50] L. Wang, J. Jiang, T. Yuan, Q. Xie, H. Liu, A. Ma, Met. Mater. Int. 26 (5) (2019) 551–563.
[51] K. Hagihara, Z. Li, M. Yamasaki, Y. Kawamura, T. Nakano, Acta Mater. 163 (2019) 226–239.
[52] Y. Chino, M. Mabuchi, S. Hagiwara, H. Iwasaki, A. Yamamoto, H. Tsubakino, Scr. Mater. 51 (7) (2004) 711–714.
[53] Z. Huang, L. Wang, B. Zhou, T. Fischer, S. Yi, X. Zeng, Scr. Mater. 143 (2018) 44–48.
[54] S. Sandlöbes, S. Zaefferer, I. Schestakow, S. Yi, R. Gonzalez-Martinez, Acta Mater. 59 (2) (2011) 429–439.
[55] M. Alvarez-Lopez, M.D. Pereda, J.A. del Valle, M. Fernandez-Lorenzo, M.C. Garcia-Alonso, O.A. Ruano, M.L. Escudero, Acta Biomater. 6 (5) (2010) 1763–1771.
[56] J. Xie, J. Zhang, Z. Zhang, Q. Yang, K. Guan, Y. He, R. Wang, H. Zhang, X. Qiu, R. Wu, Corros. Sci. 198 (2022) 110163.
[57] S. Yin, W. Duan, W. Liu, L. Wu, J. Bao, J. Yu, L. Li, Z. Zhao, J. Cui, Z. Zhang, Corros. Sci. 177 (2020) 108962.